ACS APPLIED ENERGY MATERIALS

www.acsaem.org Article

Enhanced Triboelectric Nanogenerator Performance Using Cellulose Nanocrystal-Incorporated Electrospun PVDF-HFP Nanofibrous Membranes

Hsin-Jung Kan, Cheng-Hung Chi, Ji-Wu Han, Hongta Yang, Shin-Chi Lai, Po-Hsun Chen, Po-Liang Liu, and Rong-Ho Lee*

Cite This: *ACS Appl. Energy Mater.* 2025, 8, 17530−17543 Read Online

ACCESS | Metrics & More | Article Recommendations | Supporting Information

ABSTRACT: In this study, thermoplastic polyurethane (TPU) nanofibrous membranes as the positive friction layer and cellulose nanocrystal (CNC)/poly(vinylidene fluoride-*co*-hexafluoropropylene) (CNC/PVDF-HFP) composite nanofibrous membranes as the negative friction layer were prepared by electrospinning and assembled into a triboelectric nanogenerator (TENG). Incorporating dipolar CNC nanoparticles increased the dielectric constant of the CNC/PVDF-HFP membrane and widened the work function difference with the TPU layer, enhancing charge generation during contact−separation cycles. Compared with the pristine PVDF-HFP-based TENG, the CNC/PVDF-HFP-based TENG exhibited significantly improved electrical properties. At the optimal CNC concentration, the optimized CNC/PVDF-HFP membrane achieved maximum open-circuit voltage (V_{OC}), short-circuit current density, and transferred charge of 281.5 V, 54.27 μA, and 95 nC, respectively. A maximum output power density of 5.92 W m^{-2} was achieved at an external load resistance of 19.3 MΩ. Under operating conditions of 50 N applied force at 5 Hz, the CNC/PVDF-HFP-based TENG successfully powered electronic devices such as LEDs and electronic watches, while maintaining stable V_{OC} performance over 18,000 contact−separation cycles.

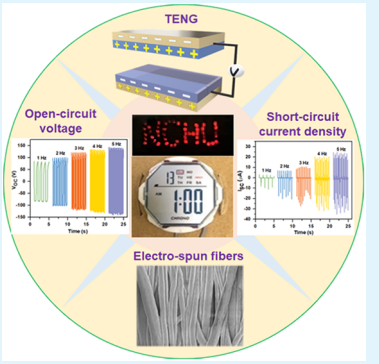

KEYWORDS: *cellulose nanocrystals, TPU, PVDF-HFP, electrospinning, triboelectric nanogenerator*

1. INTRODUCTION

Flexible and stretchable triboelectric nanogenerators (TENGs) are emerging as next-generation systems for wearable and portable electronics.[1] They have attracted significant attention due to their low fabrication cost, lightweight design, and high energy efficiency.[1] A TENG operates by coupling triboelectrification and electrostatic induction to convert mechanical motion into electrical energy. Triboelectrification can occur in various modes, including vertical contact−separation, lateral sliding, single-electrode, and freestanding triboelectric-layer modes.[2] In the contact−separation mode, the dielectric layers act as charged surfaces—one as the tribopositive, the other as the tribonegative—due to differences in electron affinity, which stem from variations in molecular and material structures. As a result, one layer donates electrons while the other accepts them, sustaining triboelectric surface charges.[3] The triboelectric polarity of a material describes its tendency to gain or lose electrons, making material selection a key factor in TENG performance. The triboelectric series ranks materials by polarity and electron affinity, providing a useful guide for selecting dielectric layer materials.[3] Generally, positive triboelectric layers are polymers containing functional groups with lone electron pairs—such as hydroxyl, amine, or amide groups. Examples include polyurethane (PU), cellulose, poly(vinyl acetate) (PVAc), poly(vinyl alcohol) (PVA), polyamide (PA), and poly(methyl methacrylate) (PMMA).[3] In contrast, negative triboelectric layers typically contain strongly electronegative functional groups, such as halogens or cyano groups. Common examples include poly(vinyl chloride) (PVC), poly(tetrafluoroethylene) (PTFE), poly(vinylidene fluoride) (PVDF), and polyacrylonitrile (PAN).[3]

Thermoplastic polyurethane (TPU) exhibits excellent flexibility, tensile strength, mechanical properties, wear resistance, breathability, and ease of melt processing. These attributes make TPU a widely used positive friction material in the construction of TENGs.[4−9] Abir et al.[10] reported an all-nanofiber-based TENG for energy harvesting and biomechanical sensing applications, fabricated via force spinning to produce TPU and PVDF nanofibrous membranes. The TPU nanofibers were coated with a homogeneously sputtered gold nanofilm, which significantly enhanced the device's output

Received: October 2, 2025
Revised: November 14, 2025
Accepted: November 18, 2025
Published: November 21, 2025

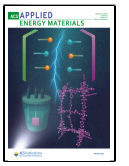

https://doi.org/10.1021/acsaem.5c03103
ACS Appl. Energy Mater. 2025, 8, 17530−17543

performance. Joo et al.[11] designed a biodegradable TPU based on polycaprolactone diol, modified with poly(dimethylsiloxane) diol and a fluorine-containing chain extender. This tailored modification simultaneously improved output performance, controlled biodegradability, and enabled the development of an eco-friendly TENG. In another study, a wearable textile triboelectric generator was fabricated by weaving PU nanofiber core-spun yarn and Si3N4-electret-incorporated PVDF nanofiber core-spun yarn into a double-layer fabric. One layer consisted of Si3N4-incorporated PVDF nanofiber fabric, while the other was PU nanofiber fabric. Under external mechanical force, the contact between these layers effectively converted mechanical energy into electrical energy.[12]

Poly(vinylidene fluoride) (PVDF) exhibits excellent electronegativity due to its high content of fluorinated groups, making it a common choice as a negative friction material in TENGs.[3] Among PVDF copolymers, poly(vinylidene fluoride)-*co*-hexafluoropropylene (PVDF-HFP) possesses the highest piezoelectric coefficient and electromechanical coupling factor.[13] It also offers good chemical stability, biocompatibility, high mechanical strength, stretchability, hydrophobicity, acid/alkali resistance, ease of processing, and wearability.[14−19] PVDF-HFP exists in five distinct crystalline phases.[20] Among them, the β-phase unit cell exhibits the highest polarization (8×10^{-30} cm), which can significantly enhance TENG output performance.[20] Various approaches have been developed to increase the β-phase content, including polarization, annealing, stretching, vapor deposition, and the incorporation of fillers.[21] The most common strategies involve doping with nanofillers and using electrospinning techniques to prepare friction materials for TENGs. Nanofiller doping introduces electron-trapping sites that facilitate charge accumulation on the friction surface while promoting β-phase formation in PVDF-HFP, thereby improving the output performance of TENGs.[22]

Cellulose, the most abundant sustainable biopolymer on Earth, is a linear polysaccharide composed of repeating D-glucose units linked by β-1,4-glycosidic bonds. Each monomer contains three hydroxyl groups, and the abundance of hydroxyl groups in cellulose chains enables the formation of van der Waals forces and hydrogen bonds between molecules, resulting in a highly ordered crystalline structure.[23−25] Natural cellulose features a unique multilayer arrangement comprising highly ordered crystalline regions and less ordered amorphous regions. Different cellulose structures can be obtained through mechanical and chemical treatments and are mainly classified into cellulose nanocrystals (CNC) and cellulose nanofibers (CNF).[26,27] CNCs are typically produced via strong acid hydrolysis, which removes amorphous regions and yields a nanocrystalline structure, while CNFs are often prepared using 2,2,6,6-tetramethylpiperidine-1-oxyl (TEMPO) oxidation.[28,29] Grafting 3-(2-aminoethylamino)propylmethyldimethoxysilane onto CNF surfaces enabled the TENGs to achieve both high output performance and hydrophobicity, thereby allowing them to function effectively for monitoring human physical activity under perspiration conditions.[30] CNCs were extracted from recycled waste paper and used to fabricate a water-soluble CNC/methylcellulose film that can be directly applied to the positive electrode human skin as a wearable TENG.[31] CNCs were embedded into PDMS films, where the positive surface charges of CNCs generated an additional electric field that promoted induced charge formation and enhanced the TENG's output performance.[32] A TENG was fabricated using a CNC/gelatin composite film as the positive friction layer and a PTFE film as the negative friction layer to monitor athletes' posture and movements during jump training.[33] TENGs employing CNCs as triboelectric layers in a single-electrode configuration, integrated with graphene electrodes and paired with nitrile or PTFE as counter triboelectric layers, have been investigated.[34] The TENG efficiently harvested biomechanical energy from piano playing and successfully stored the generated energy in a capacitor for powering various electronic devices. A cellulose-based TENG with a fiber−wave−arch structure was fabricated via a multifluid electrospinning process for applications in air filtration and wind sensing.[35] The device also exhibited excellent formaldehyde removal capability, achieving a 92% filtration efficiency at 0.25 mg m^{-3}. These results demonstrate the great potential of this TENG for use in self-powered sensing applications.

In this study, a TPU nanofibrous membrane was fabricated as the positive friction layer, and CNC/PVDF-HFP composite nanofibrous membranes were fabricated as the negative friction layer via electrospinning, then assembled into a TENG. The electrospinning process produced flexible nanofibrous membranes with excellent surface roughness, high porosity, outstanding wear resistance, and good breathability, enabling their application in wearable TENGs.[19] During electrospinning, uniaxial stretching of polymer chains and electric field-induced polarization promoted the formation of the β-phase in PVDF-HFP, which possesses the highest spontaneous polarization, thereby increasing the surface charge density of the friction material.[19,36] Alignment of PVDF-HFP nanofibers was achieved by increasing the rotational speed of the drum collector, further enhancing the β-phase content.[37,38] Incorporating dipolar CNC into the PVDF-HFP nanofibrous membrane introduces hydrogen bonding between CNC and PVDF-HFP, which enhances the dielectric constant and improves the TENG output performance. SEM and TEM analyses revealed that fiber diameter increased with CNC content, while TEM provided detailed morphological observations of the CNC/PVDF-HFP nanofibers. XRD and FTIR analyses were used to investigate the crystallization characteristics of the membranes. Kelvin probe force microscopy (KPFM) measurements indicated that the work function (Φ) differences between the TPU-based positive triboelectric layer and the CNC/PVDF-HFP-based negative triboelectric layer increased with higher CNC content, thereby facilitating enhanced charge generation during the contact−separation cycles. The CNC/PVDF-HFP-based TENGs exhibited superior triboelectric output compared to those based solely on PVDF-HFP membranes. The optimized CNC/PVDF-HFP membrane achieved maximum open-circuit voltage (V_{OC}), short-circuit current density (I_{SC}), and transferred charge of 281.5 V, 54.27 μA, and 95 nC, respectively. Under a 50 N force at 5 Hz contact frequency, the TENG successfully powered electronic devices such as LEDs and electronic watches, and maintained stable Voc after 18,000 contact−separation cycles.

2. EXPERIMENTAL DETAILS

2.1. Chemicals. *N*,*N*-Dimethylformamide (DMF) and tetrahydrofuran (THF) were purchased from Aldrich. Cellulose nanocrystals (CNCs; diameter: 10−20 nm, length: 300−900 nm) were obtained from Nanografi Nano Technology and used as received. Thermoplastic polyurethane (TPU; Mn = 90,000 g·mol^{-1}, Mw = 200,000 g·mol^{-1}) pellet was purchased from Covestro Ltd., and poly(vinylidene

https://doi.org/10.1021/acsaem.5c03103
ACS Appl. Energy Mater. 2025, 8, 17530−17543

fluoride)-*co*-hexafluoropropylene (PVDF-HFP; Mn = 130,000 g·mol^{-1}, Mw = 400,000 g·mol^{-1}) pellet was purchased from Sigma-Aldrich.

2.2. Preparation of TPU and CNC/PVDF-HFP Solutions for Electrospinning. TPU pellets (1.2 g) were added to a DMF/THF mixed solvent (8.8 mL, 1:1 v/v) and stirred at 300 rpm at 60 °C for 12 h to obtain the electrospinning solution. A mixed solvent system of DMF and THF was used because TPU consists of hard and soft segments with markedly different polarities; therefore, solvents with different characteristics are required to act synergistically to achieve uniform dissolution. In addition, CNC powders with different weight ratios (0.5, 1.0, 1.5, and 2.0 wt % relative to PVDF-HFP) and PVDF-HFP (2.832 g) were added to DMF (12 mL) and stirred at 300 rpm at 70 °C for 4 h. The resulting CNC/PVDF-HFP solutions were then used for the preparation of the nanofibrous membranes.

2.3. Preparation of TPU and PVDF-HFP Based Electro-Spun Nanofibrous Membranes. The TPU nanofibrous membrane was fabricated using vertical electrospinning equipment (FES-COS, Taiwan). The TPU electrospinning solution was loaded into a plastic syringe equipped with a 21-gauge stainless steel needle. The solution was delivered at a constant flow rate of 1.4 mL h^{-1} using a syringe pump (NE-300 Just Infusion). The electrospinning nozzle was moved laterally over a distance of 18 cm at a speed of 4.5 cm s^{-1}. A voltage of 8.5 kV was applied, with a tip-to-collector distance of 14 cm, and fibers were collected on a baking paper wrapped stationary metal plate (25 × 25 cm^2; baking paper thickness ∼0.5 mm) for 4 h. The electrospinning process was carried out at 26.5 ± 2.5 °C and 47 ± 5% relative humidity (RH). The obtained TPU membranes were dried in an oven at 60 °C for 6 h. A photograph of the TPU membrane is shown in Figure S1a.

For CNC/PVDF-HFP nanofibrous membranes, the CNC/PVDF-HFP solution was loaded into a syringe with a 21-gauge stainless steel needle and fed at 1.4 mL h^{-1}. A voltage of 14 kV was applied, with a tip-to-collector distance of 14 cm. Fibers were collected for 4 h on a baking paper wrapped rotating drum (1500 rpm) to obtain aligned nanofibers. The process was conducted under the same temperature and RH conditions as above, and CNC/PVDF-HFP membranes were dried at 60 °C for 6 h. A photograph of the CNC/PVDF-HFP membrane is shown in Figure S1b.

2.4. Characterization of TPU and CNC/PVDF-HFP Nanofibrous Membranes. Fourier transform infrared (FTIR) spectra were recorded using a HORIBA FT-720 spectrometer. The glass transition temperature (T_g) and melting temperature (T_m) of CNC/PVDF-HFP nanofibrous membranes were determined by differential scanning calorimetry (DSC, TA Instruments DSC-2010) and thermogravimetric analysis (TGA, TA Instruments TGA-2050). Additional TGA measurements were performed using a PerkinElmer Pyris system to determine the thermal decomposition temperature (T_d), defined as the temperature corresponding to 5% weight loss, for CNC powder and CNC/PVDF-HFP nanofibrous membranes. TGA analyses were conducted in a nitrogen atmosphere at a heating rate of 10 °C min^{-1}. The particle size distribution of CNCs (0.5 mg) in 8 mL of DMF solvent was measured using the dynamic light scattering (DLS) method (Litesizer DLS 100). The DLS sample was prepared by subjecting the CNC solution to ultrasonic treatment at room temperature for 2 h. The tensile test of CNC/PVDF-HFP membranes specimens was conducted using a testing machine (GOTECH, AI-3000). The tests were performed at a load speed of 10 mm/min.

The water contact angles (CAs) of TPU and CNC/PVDF-HFP nanofibrous membranes were measured using a Kyowa DropMaster optical contact angle meter. Surface morphologies were examined by cold field emission scanning electron microscopy (FESEM; Hitachi-4800) operated at 1.5−2.0 kV. High-resolution transmission electron microscopy (HRTEM, JEOL JEM-1400Flash, Japan) operated at 200 kV was used to observe the morphology of CNC/PVDF-HFP nanofibrous membranes, which were collected on Cu grids. The crystalline structures of the membranes were characterized by X-ray diffraction (XRD, Shimadzu SD-D1) using a Cu target at 35 kV and 30 mA. The interactions between CNC and PVDF-HFP were analyzed by X-ray photoelectron spectroscopy (XPS, ESCALAB 250Xi, Thermo Fisher Scientific). The surface roughness (R_a), contact potential difference (CPD), and Φ of the nanofibrous films were measured using KPFM (Bruker, Dimension Icon).

2.5. First-Principles Calculations. To elucidate how CNC incorporation modifies the surface electronic structure and enhances the triboelectric performance of PVDF-HFP-based friction layers, first-principles calculations were carried out using the Vienna *ab-initio* Simulation Package (VASP).[39−41] The exchange−correlation functional was treated using the generalized gradient approximation (GGA-PW91).[42,43] Projector augmented wave (PAW) potentials were used, with a plane-wave cutoff energy of 450 eV. The supercell dimensions for the PVDF-HFP single-chain model were chosen based on the fully relaxed geometry of a $(C_5F_8H_2)_{10}$ polymer segment. After structural optimization, the chain length extended to approximately ≈ 50 Å, and the lateral chain thickness stabilized around ≈ 8 Å. A vacuum spacing of c = 30 Å was introduced along the z-direction to avoid interactions between periodic images. The resulting supercell of PVDF-HFP contains 150 atoms. The PVDF-HFP + CNC interfacial model was constructed using the fully relaxed geometry of an $(C_5F_8H_2)_8$ polymer segment interacting with a simplified CNC fragment $(C_{12}O_{10}H_6)_1$. After structural optimization, the combined system extended to approximately ≈ 53 Å along the polymer backbone direction, while the lateral dimension converged to ≈ 10 Å to accommodate the CNC-induced structural expansion. A vacuum spacing of c = 30 Å was added perpendicular to the interface to eliminate periodic interactions. The resulting supercell of CNC/PVDF-HFP contained 148 atoms. A 1 × 1 × 1 Monkhorst−Pack k-point grid was used for all calculations due to the large supercell size and the nonperiodic nature of the polymeric models. The CNC fragment remains structurally intact after optimization, retaining its ring-like carbon−oxygen framework without distortion or breakdown, as illustrated in Figure 1. It is positioned close to the PVDF-HFP chain, and the two components adopt a stable geometrical arrangement in which neither excessive twisting nor steric repulsion is observed. The overall configuration indicates that both the CNC segment and the PVDF-HFP chain maintain stable atomic structures under the applied optimization conditions.

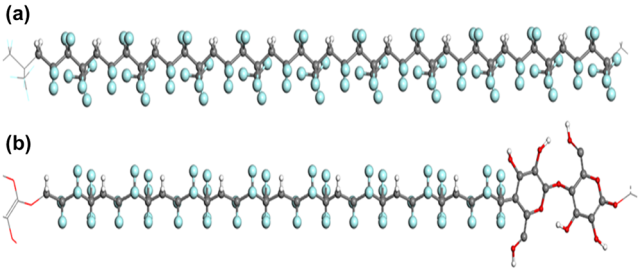

Figure 1. Shows the optimized structures of (a) the PVDF-HFP chain and (b) the CNC/PVDF-HFP model. In both models, hydrogen atoms are shown in white, carbon atoms in gray, fluorine atoms in light blue, and oxygen atoms in red. The CNC fragment is positioned near the PVDF-HFP chain, allowing the optimized geometry of the combined system to be obtained.

2.6. Fabrication of the TPU and CNC/PVDF-HFP Nanofibrous Membranes Based TENGs. The architecture of the TPU- and CNC/PVDF-HFP-based nanofibrous membrane TENGs is shown in Figure 2. To fabricate the TENG, TPU and CNC/PVDF-HFP nanofibrous membranes (3.0 × 2.0 cm^2, average thickness ∼0.3 mm) were cut and affixed to commercially available copper (Cu) foil tapes, which served as electrodes for the positive and negative friction layers. Each triboelectric-layer-adhered Cu foil was then attached to a polypropylene (PP) substrate using double-sided adhesive tape. The two PP substrates bearing the positive and negative triboelectric layers were assembled into a TENG device using four PU foam spacers, with a separation distance of approximately 10 mm between them.

2.7. Triboelectric Characterization of the TENGs. The V_{OC} was measured using a Keithley 6514 electrometer, while the I_{SC} was

https://doi.org/10.1021/acsaem.5c03103
ACS Appl. Energy Mater. 2025, 8, 17530−17543

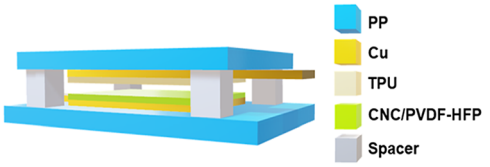

Figure 2. Architecture of the TPU and CNC/PVDF-HFP nanofibrous membranes based TENG.

recorded via an oscilloscope connected to a Stanford Research Systems SR570 current preamplifier. A LinMot linear motor system supplied a stable external force to induce reciprocating contact between the TPU- and PVDF-HFP-based electrodes. Dynamic mechanical pressure was applied using a Montrol motion control system (MSP 50072) under various forces (10−60 N) and frequencies (1−10 Hz). To simulate actual operating conditions, the contact−separation distance between the triboelectric layers was fixed at 10 mm. Transferred charge was measured with the Keithley 6514 electrometer. All measurements were performed under ambient conditions.

3. RESULTS AND DISCUSSION

3.1. Morphology of the CNC Nanoparticles. Both crystalline and amorphous regions are present in cellulose. In the crystalline domains, variations in molecular orientation and hydrogen bonding networks give rise to different cellulose polymorphs. Four polymorphic forms of cellulose have been identified: cellulose I, cellulose II, cellulose III, and cellulose IV.[44] In this study, the CNC used corresponds to the cellulose I polymorph.[45] The SEM image indicates that the CNC particles possess widths of approximately 10−20 nm and lengths of 100−300 nm.[45] Figure S2 shows the particle size distribution of CNC dispersed in DMF, revealing particle sizes ranging from 125 to 375 nm. Good dispersibility of CNCs in DMF was observed.

3.2. Thermal Properties of TPU and CNC/PVDF-HFP Nanofibrous Membranes. As shown in Figure S3a, the TGA thermograms indicate that CNC exhibits lower thermal stability than both random and aligned PVDF-HFP nanofibrous membranes. The CNC powder shows approximately 8% weight loss below 125 °C, attributed to moisture absorption, with maximum degradation occurring at around 310 °C. In contrast, the T_d of aligned PVDF-HFP nanofibrous membranes is similar to that of random membranes, with maximum weight loss observed at ∼455 °C, corresponding to PVDF-HFP backbone degradation. For aligned CNC/PVDF-HFP membranes (APCNC-0.5, APCNC-1.0, APCNC-1.5, and APCNC-2.0), T_d and char yield exhibit only slight variations with increasing CNC content. Figure S3b shows the DSC thermograms of PVDF-HFP and aligned CNC/PVDF-HFP membranes. The T_g and T_m of the pristine PVDF-HFP pellets were observed at approximately 120 and 140 °C, respectively. The T_g and T_m of the CNC/PVDF-HFP membranes slightly decreased, which can be attributed to the plasticizing effect of CNCs within the PVDF-HFP matrix. The melting enthalpy of CNC/PVDF-HFP membranes shows minor differences compared to PVDF-HFP membrane, likely due to slight variations in crystallinity of the PVDF-HFP matrix.

3.3. Morphologies and Mechanical Properties of the CNC/PVDF-HFP Nanofibrous Membranes. The morphology and fiber diameter distributions of TPU, random PVDF-HFP, and aligned PVDF-HFP nanofibrous membranes are shown in Figure S4. TPU nanofibers exhibited significantly larger diameters (1200−1500 nm) compared to random PVDF-HFP (150−400 nm) and aligned PVDF-HFP (250−500 nm) nanofibers. The polymer chains of TPU are relatively long and contain hydrogen bonding interactions between the hard and soft segments, resulting in strong intermolecular forces, high viscosity, and high elasticity of the solution. The high viscosity prevents the electrospinning jet from being stretched into fine fibers, leading to a larger fiber diameter. In contrast, PVDF-HFP exhibits relatively lower viscosity, allowing the solution to be more easily stretched by the applied electric field to form finer fibers, resulting in a smaller fiber diameter. SEM images revealed well-defined unidirectional alignment for aligned PVDF-HFP nanofibers (Figure S4c). Similarly, aligned CNC/PVDF-HFP nanofibers (APCNC-0.5, APCNC-1.0, APCNC-1.5, APCNC-2.0) showed good unidirectional alignment, with diameters increasing progressively from 300 to 1650 nm as CNC content increased (Figures 3 and S5). SEM, TEM, and EDX analyses of APCNC-1.0 confirmed the uniform distribution of CNC particles throughout the PVDF-HFP nanofibrous matrix (Figures 4 and S6).

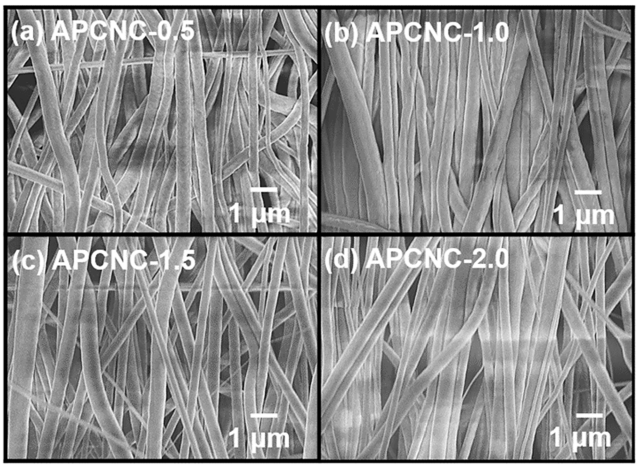

Figure 3. SEM images of (a) APCNC-0.5, (b) APCNC-1.0, (c) APCNC-1.5, and (d) APCNC-2.0 nanofibrous membranes.

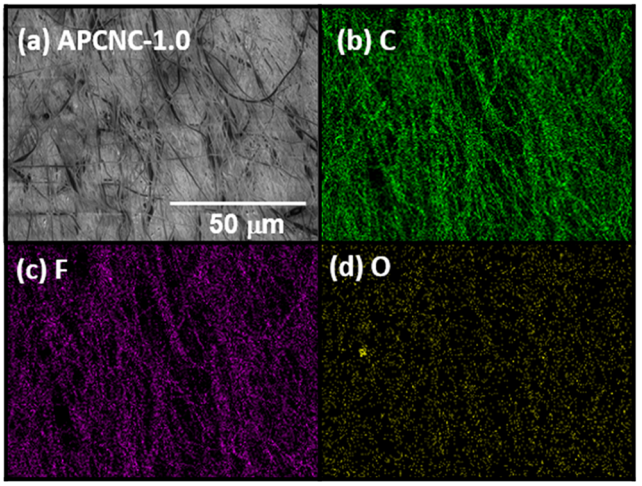

Figure 4. (a) SEM image and (b−d) EDX images of (b) C, (c) F, and (d) O in the APCNC-1.0 nanofibrous membranes.

https://doi.org/10.1021/acsaem.5c03103
ACS Appl. Energy Mater. 2025, 8, 17530−17543

To further examine the distribution of CNC nanoparticles within the CNC/PVDF-HFP nanofibrous membranes, TEM images of the PVDF-HFP, APCNC-1.0, and APCNC-2.0 samples are shown in Figure S7. The TEM image revealed that the surface of the PVDF-HFP fibers was smooth, and the fiber diameters exhibited little variation (Figure S7a). In contrast, the surface of the CNC/PVDF-HFP nanofibrous membrane appeared rough, and the fiber diameters were less uniform because the CNCs were embedded within the PVDF-HFP fibers (Figure S7b,c). Defects caused by CNC aggregation were observed inside the fibers of the APCNC-2.0 membrane (Figure S7d). Furthermore, the SEM images showed that the CNCs had a diameter of approximately 30 nm, which was much smaller than that of the PVDF-HFP fibers. Moreover, XPS results confirmed strong intermolecular interactions between CNC and PVDF-HFP, allowing CNCs to be uniformly embedded and distributed within the PVDF-HFP fibers. Nevertheless, the CNC nanoparticles were not clearly visible in the TEM images owing to the limited penetration of the supporting membrane.

The hydrophobicity of TPU, PVDF-HFP, and CNC/PVDF-HFP nanofibrous membranes was evaluated using contact angle (CA) measurements, with representative photographs shown in Figure S8. The CAs of the CNC/PVDF-HFP membranes decreased with increasing CNC content, indicating enhanced hydrophilicity. The enhancement of the hydrophobicity of the CNC/PVDF-HFP membranes is not favorable for triboelectrification.

To investigate the effect of CNCs on PVDF-HFP, stress–strain curves were measured (Figure S9). The aligned PVDF-HFP membrane exhibited significantly higher tensile stress than the random membrane due to the unidirectional fiber alignment. Moreover, the tensile stress of the CNC/PVDF-HFP composite membranes decreased with increasing CNC content. The incorporated CNCs act as plasticizers, disrupting the packing of polymer chains and consequently reducing tensile strength. The tensile strain of the CNC/PVDF-HFP membranes strongly depends on the CNC loading. At low concentrations (<1.5 wt %), well-dispersed CNCs enhance strain owing to their plasticizing effect. The tensile performance reaches its maximum at 1.5 wt % CNC; however, further increasing the CNC content to 2.0 wt % leads to agglomeration, resulting in decreased strain.[46]

3.4. Crystal Structure of CNC/PVDF-HFP Nanofibrous Membranes. As shown in Figure S10, the characteristic absorption bands of the TPU fibers observed include the C═O stretching of the amide group at 1729 cm^{-1}, O–C–N stretching in the range of 1530–1595 cm^{-1}, N–H bending at 1260 cm^{-1}, and N–H stretching vibrations at 3325 cm^{-1}. Other notable characteristic bands were also identified, such as the alkane – CH_2 stretching between 3050–2818 cm^{-1}, C–N and C–O stretching at 1226 and 1163 cm^{-1}, respectively, and ester C–O–C symmetrical stretching vibrations at 1074 cm^{-1}.[47]

Figure S11 shows the FTIR spectra of CNC powder, random PVDF-HFP, aligned PVDF-HFP, and CNC/PVDF-HFP (CNC/APCNC, APCNC-0.5, APCNC-1.0, APCNC-1.5, and APCNC-2.0) nanofibrous membranes. The main functional groups of the CNC powder are as follows: the peak at 2902 cm^{-1} corresponds to C–H stretching vibrations; the peak at 1035 cm^{-1} corresponds to C–O stretching vibration; the peaks at 1058, 1109, and 1162 cm^{-1} correspond to C–O–C stretching vibrations; and the peak at 3340 cm^{-1} corresponds to O–H stretching vibrations.[48−51] The random PVDF-HFP, aligned PVDF-HFP, and CNC/PVDF-HFP nanofibrous membranes are composed of a nonpolar α-phase, associated with the peak at 761 cm^{-1}, and a β-phase, associated with the peaks at 838, 879, 1069, 1177, 1272, and 1402 cm^{-1}. Absorption bands corresponding to CH_2 wagging (1402 cm^{-1}), symmetric CF_2 stretching (1177 cm^{-1}), and out-of-plane γ-CF_3 stretching (1069 cm^{-1}) were observed in the PVDF-HFP nanofibrous membranes. A small hump at 1272 cm^{-1} was attributed to symmetric CF_2 vibrations. The bands related to the amorphous β-phase at 879 and 838 cm^{-1} were also present, indicating the amorphous nature of the nanofibrous membranes. Additionally, the absorption peak at 761 cm^{-1} corresponds to the nonpolar α-phase and is attributed to the bending vibration of $-CF_2$ groups within the α-phase structure..[52,53] For the CNC/PVDF-HFP nanofibrous membranes, the intensity of the absorption peaks corresponding to the α- and β-phases did not change significantly with increasing CNC content, which is attributed to the low doping level of CNC.

As shown in Figure S12, a broad band at 2θ = 20.4° corresponds to the amorphous phase of the TPU nanofibrous membrane.[54,55] The XRD patterns of CNC powder, PVDF-HFP pellets, random PVDF-HFP, aligned PVDF-HFP, and CNC/PVDF-HFP nanofibrous membranes are presented in Figure 3. The CNC powder exhibits diffraction peaks at approximately 2θ = 14.5°, 16.5°, and 22.5°, corresponding to the (110), (110), and (200) planes, respectively, which are characteristic of cellulose I.[45] For the PVDF-HFP pellet, the diffraction peaks at 2θ = 18.1° (100) and 26.3° (021) correspond to the α phase, while the peak at 2θ = 19.6° is assigned to the crystalline β phase (Figure 5). The intensities

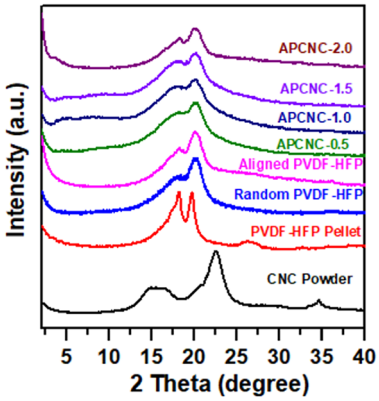

Figure 5. XRD images of the CNC powder, PVDF-HFP pellet, random PVDF-HFP, aligned PVDF-HFP, and CNC/PVDF-HFP nanofibrous films.

of the α-phase peak at 2θ = 18.1° and the β-phase peak at 2θ = 19.6° are nearly equal in the PVDF-HFP pellet. Compared with the PVDF-HFP pellet, both random and aligned PVDF-HFP nanofibrous membranes exhibit a higher intensity for the β-phase diffraction peak relative to the α-phase peak. Furthermore, both peaks become broader and shift to higher diffraction angles. The crystalline phases of CNC/PVDF-HFP nanofibers with various CNC contents were further analyzed. Peak deconvolution in the 2θ range of 12–25° was performed using the FitPeaks(Pro) function in OriginPro (Figure S13). PVDF-HFP primarily exhibits nonpolar α-phase peaks at 2θ = 17.8° (100), 18.2° (020), and 20.1° (110), along with a polar

https://doi.org/10.1021/acsaem.5c03103
ACS Appl. Energy Mater. 2025, 8, 17530−17543

β-phase peak at 2θ = 20.2° (110:200).[56] The effect of CNC incorporation on the crystalline structure of CNC/PVDF-HFP nanofibrous membranes is summarized in Table S1. With the addition of CNC, the proportion of the α phase increases, while the β (110:200) phase content slightly decreases.[56] This indicates that CNC incorporation inhibits β-phase formation while promoting α-phase growth. CNCs are encapsulated within the nanofibers, and secondary interactions between the −OH groups of CNC and the F atoms in PVDF-HFP reduce the amorphous phase content.[57,58]

3.5. Surface Morphologies and Electronic Properties of the TPU and CNC/PVDF-HFP Nanofibrous Membranes. In order to study the surface morphology and electronic properties of the triboelectric layers, the surface roughness and surface potential of the TPU, aligned PVDF-HFP, and CNC/PVDF-HFP nanofibrous films were measured using KPFM spectroscopy. The KPFM images of the TPU, aligned PVDF-HFP, and CNC/PVDF-HFP nanofibrous films are shown in Figure S14. The R_a, CPD, and Φ values of the nanofibrous films are summarized in Table 1. The results

Table 1. Surface Roughness (R_a), Contact Potential Difference (CPD), and Work Function (Φ) of Aligned PVDF-HFP, and CNC/PVDF-HFP Nanofibrous Membranes

Sample	R_a (nm)	V_{CPD} (V)	Φ (eV)
TPU	4.35 ± 0.15	0.41 ± 0.11	5.19 ± 0.12
aligned PVDF-HFP	7.48 ± 0.23	−0.65 ± 0.22	6.25 ± 0.13
APCNC-0.5	9.68 ± 0.27	−0.94 ± 0.18	6.54 ± 0.11
APCNC-1.0	9.52 ± 0.32	−1.12 ± 0.15	6.72 ± 0.08
APCNC-1.5	9.78 ± 0.25	−1.33 ± 0.12	6.95 ± 0.18
APCNC-2.0	10.25 ± 0.34	−1.49 ± 0.16	7.09 ± 0.12

indicated that the surface roughness of the aligned PVDF-HFP films was slightly higher than that of the TPU films. Moreover, the surface roughness increased with increasing CNC content in the CNC/PVDF-HFP nanofibrous films. The higher surface roughness of the triboelectric layer promotes enhanced charge generation in the TENGs. In addition, the CPD values of the TPU, aligned PVDF-HFP, APCNC-0.5, APCNC-1.0, APCNC-1.5, and APCNC-2.0 nanofibrous films were 0.41, −0.65, −0.94, −1.12, −1.33, and −1.49 V, respectively, while their corresponding Φ values were 5.19, 6.25, 6.54, 6.72, 6.95, and 7.09 eV. The CPD and Φ differences between the TPU-based positive triboelectric layer and the CNC/PVDF-HFP-based negative triboelectric layer increased with higher CNC content, which facilitated enhanced charge generation during the contact−separation cycles.

3.6. Electrostatic Potential Analysis of PVDF-HFP and CNC/PVDF-HFP Models. Figure 6 presents the electrostatic potential profiles of the optimized PVDF-HFP and CNC/PVDF-HFP models. The maximum (blue), average (red), and minimum (green) potential curves are plotted along the z-direction, allowing a direct visualization of how the incorporation of CNC influences the potential distribution within the molecular region and the vacuum level. By comparing the two systems, a stable vacuum plateau is observed in the smoothest section (gray area), indicating sufficient vacuum spacing and a well-defined reference vacuum level. Within the molecular region, the average and minimum potentials exhibit notable variations, reflecting the spatial distribution of atomic positions in the model. Comparing the

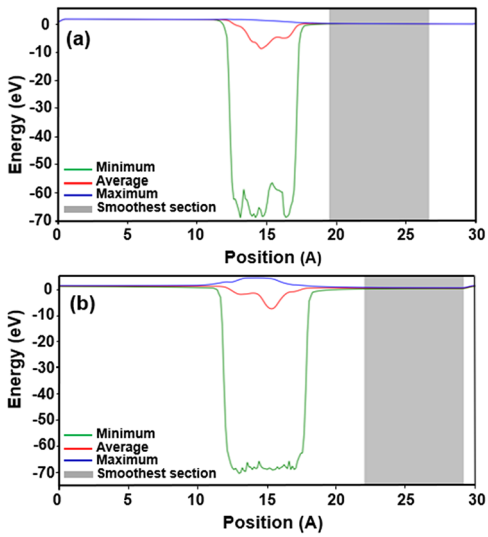

Figure 6. Electrostatic potential profiles of (a) PVDF-HFP and (b) CNC/PVDF-HFP models. The maximum (blue), average (red), and minimum (green) potential values along the z-direction are shown. The smoothest section (gray area) indicates the region where the vacuum potential becomes flat and stable. In both systems, the convergence of the three curves in the vacuum region confirms a well-defined vacuum level, while differences in the internal potential curvature reflect the distinct structural configurations of the two models.

two plots, the CNC/PVDF-HFP model displays slightly different potential curvature in the molecular region relative to the pure PVDF-HFP model. It is noted that the maximum and minimum curves correspond to the pointwise extremum values among all $V(x,y,z)$ grid points on a given slice perpendicular to the z direction. Here, $V(x,y,z)$ represents the electrostatic potential sampled on the real-space grid, which corresponds to the local potential energy at each point in the simulation cell. It reflects contributions from nuclei, electrons, and the exchange−correlation potential. In contrast, the red curve represents the plane-averaged electrostatic potential $\tilde{V}(z)$, obtained by integrating $V(x,y,z)$ over the entire xy-plane and dividing by the plane area. Because these quantities arise from fundamentally different statistical operations—pointwise extrema versus an area-averaged value—the average curve does not necessarily lie between the maximum and minimum curves. In regions containing atoms, substantial spatial variation in $V(x,y,z)$ can result in significant differences between local extrema and the integrated average value. In the vacuum region, however, the electrostatic potential becomes nearly uniform across the plane, causing the maximum, average, and minimum curves to converge to the same flat plateau.

The work function was calculated using the relation $\Phi = E_{vac} - E_F$, where E_{vac} is extracted from the flat vacuum plateau in the electrostatic potential profile, and E_F is the Fermi level obtained from the DFT calculation. The smoothed potential $\tilde{V}(z)$ was used to align the electrostatic reference levels and determine E_{vac}. From the potential plateau in the PVDF-HFP model, E_{vac} is identified as approximately 0.101 eV, whereas in the CNC/PVDF-HFP model, the plateau occurs at around 0.036 eV. The values of E_F are −3.593 eV for PVDF-HFP and −4.309 eV for CNC/PVDF-HFP, leading to work functions of 3.694 and 4.345 eV, respectively. The increase of $\Delta\Phi$ = 0.651 eV indicates that the incorporation of CNC enhances the

https://doi.org/10.1021/acsaem.5c03103
ACS Appl. Energy Mater. 2025, 8, 17530−17543

electron-trapping capability at the surface, allowing charge retention and contributing to the improved triboelectric output of the TENG device. This trend is consistent with the local potential profiles, where the CNC-containing model exhibits a more pronounced potential modulation along z, which may be associated with enhanced interfacial polarization.

3.7. Dielectric Constants of the CNC/PVDF-HFP Nanofibrous Membranes. The surface charge density of the triboelectric layer is positively correlated with its dielectric constant, indicating that an increase in the dielectric constant of the triboelectric layer can effectively enhance the triboelectric performance of the TENG.[59,60] The dielectric constant as a function of frequency for the CNC/PVDF-HFP membranes is shown in Figure S15. The dielectric constant of the PVDF-HFP membrane increased upon the incorporation of the CNC. The hydrogen bonding between the hydroxyl (−OH) groups on the surface of CNCs and the fluorine (F) atoms on the polymer chains of PVDF-HFP can form dipoles that respond to the applied electric field. The large dipole moments associated with these hydrogen bonds are a key factor contributing to the enhanced dielectric constant of the CNC/PVDF-HFP composite membrane. The presence of hydrogen bonding between CNC and PVDF-HFP thus promotes an increase in the dielectric constant of the composite membrane.[61] However, when the CNC concentration exceeds the percolation threshold, the dielectric constant decreases due to the disruption of the β-phase in PVDF-HFP. In addition, the incorporation of dipolar CNC nanoparticles into PVDF-HFP induces interfacial polarization, which enhances the dielectric constant. However, when CNCs aggregate, the dielectric constant decreases because the effective interfacial area is reduced. Therefore, a lower dielectric constant was observed for the APCNC-2.0 sample.[59]

3.8. Electrical Characteristics of the CNC/PVDF-HFP Nanofibrous Membranes Based TENGs. The schematic illustration and electrical power generation stages of a vertical contact-separation mode TENG (Figure 7).[1] At the beginning, the positive and negative triboelectric layers remain separated, and no net charges have been established on either layer (Figure 7a). When triboelectric layers with different electron affinities are brought into contact under an external force, opposite charges are generated on their surfaces due to contact electrification (Figure 7b). The surface of TPU, which tends to lose electrons, becomes positively charged, while CNC/PVDF-HFP, which has a higher tendency to gain electrons, becomes negatively charged. After the electron exchange between the surfaces of the triboelectric layers reaches equilibrium, the total amount of charge on both surfaces remains constant. When the applied force on the TENG is released (releasing stage), the surfaces of the triboelectric layers separate from each other due to the restoring and pulling forces, thereby disturbing the charge balance (Figure 7c). At this stage, the triboelectric layers carrying opposite charges generate an electric potential difference between the electrodes through electrostatic induction, and a current flow through the external circuit connecting the electrodes under the closed-circuit condition. After a certain period, as electrons flow through the external conductor, the electric potential difference between the electrodes gradually decreases, and consequently, the current flow ceases (Figure 7d). When the triboelectric layers are brought closer to each other by an external force, a reversed electric potential difference is established between the electrodes, causing electrons to flow in the opposite direction and generating an electric current once again (Figure 7e). After the triboelectric layers come into full contact, the electric potential difference becomes zero, and the electron flow ceases. In this manner, an alternating current is produced as a result of the periodic contact−separation motion of the triboelectric layers.[1]

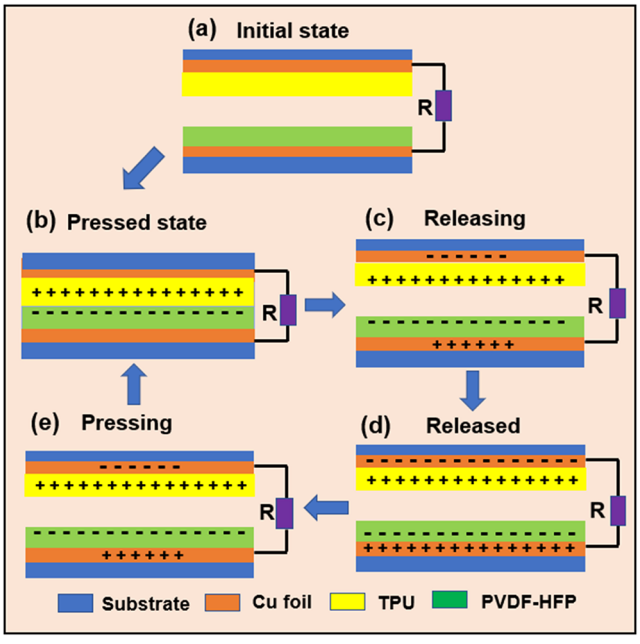

Figure 7. Schematic illustration of the working mechanism of the TENG device.

The energy generated by a TENG is positively correlated with the amount of charge that the friction materials can capture and store. Typically, factors such as the material properties, the effective contact area between the friction layers, the contact frequency, and the externally applied mechanical force all influence the output performance of the TENG. As shown in Figures S16 and S17, the contact frequency was fixed (5 Hz), and the effects of different applied forces (10−60 N) on the V_{OC} and I_{SC} of the TENGs were measured. The V_{OC} and I_{SC} values of the CNC/PVDF-HFP nanofibrous membranes based TENGs are summarized in Tables S2 and S3. Both the V_{OC} and I_{SC} increased with increasing applied force. This is mainly because, under applied force, the friction layer is compressed, thereby increasing the effective contact area and enhancing the amount of accumulated charge. Additionally, higher applied force increases the elastic deformation of the friction layer, which further increases the capacitance of the CNC/PVDF-HFP TENG and enhances charge storage. Applying greater force also promotes the generation of more surface triboelectric charges, thereby improving the electrical output. However, when the applied force reaches 60 N, it exceeds the mechanical tolerance of the nanofibrous membranes, causing surface damage, which results in a decrease in overall electrical performance. Compared to the random PVDF-HFP-based TENG, the aligned PVDF-HFP-based TENG exhibited higher V_{OC} and I_{SC} values. Furthermore, for the CNC/PVDF-HFP-based TENGs, V_{OC} and I_{SC} increased with rising CNC content. The highest V_{OC} (53.0 V) and I_{SC} (289.2 μA) values were achieved with the APCNC-1.0-based TENG. However, excessive CNC content led to reduced V_{OC} and I_{SC} values,

https://doi.org/10.1021/acsaem.5c03103
ACS Appl. Energy Mater. 2025, 8, 17530−17543

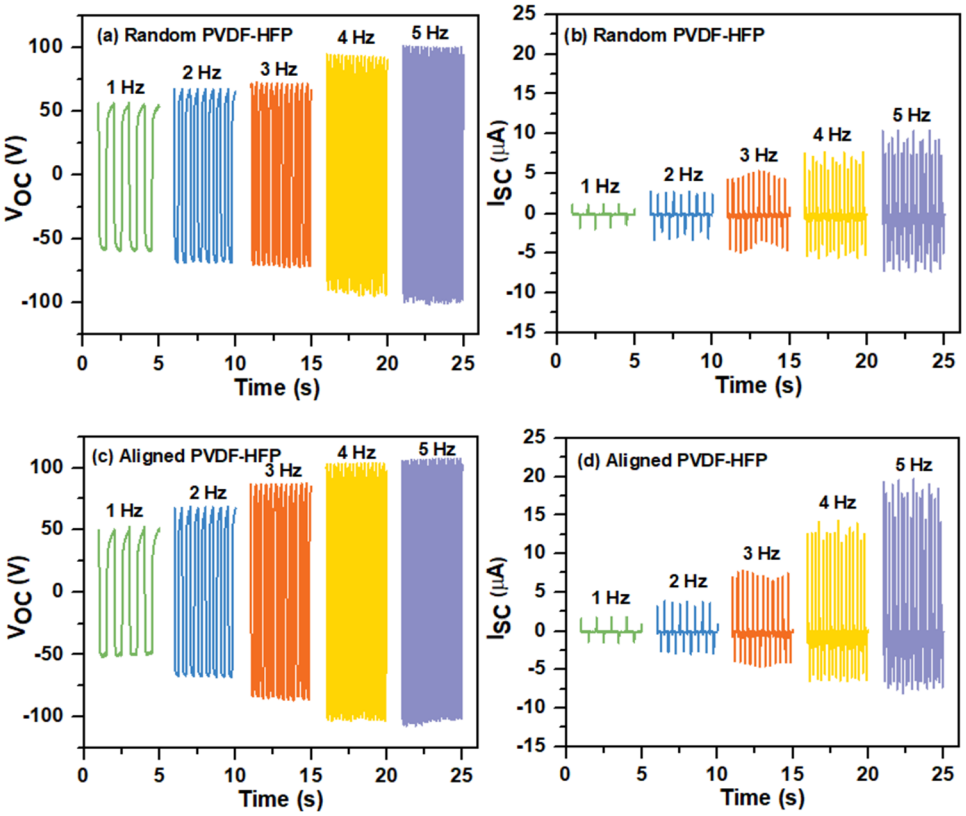

Figure 8. V_{OC} and I_{SC} of the TENGs measured at 50 N under various applied frequencies [(a), (b): Random PVDF-HFP TENG; (c), (d): Aligned PVDF-HFP TENG].

as observed in the APCNC-1.5 and APCNC-2.0-based TENGs.

Subsequently, under a fixed applied mechanical force, the effects of varying contact frequencies on the V_{OC} and I_{SC} of the TENGs were investigated. As shown in Figures 8 and 9 and summarized in Tables S4 and S5, higher contact frequencies led to increased V_{OC} and I_{SC} values. This enhancement is primarily attributed to the higher contact−separation frequencies accelerating the rate of electron transfer, allowing charges to move more rapidly.[62] The highest V_{OC} and I_{SC} values were observed for all the CNC/PVDF-HFP nanofibrous membranes-based TENGs at a frequency of 5 Hz under an applied force of 50 N.

The V_{OC}, I_{SC}, and transferred charge values of the pristine PVDF-HFP- and CNC/PVDF-HFP-based TENGs were measured at 5 Hz under an applied force of 50 N (Figure 10). The enhanced performance of the aligned PVDF-HFP compared with the random PVDF-HFP can be attributed to two primary factors. First, FT-IR analysis confirmed a higher β-phase content in the aligned PVDF-HFP, which contributes to improved electrical output. Second, the alignment of nanofibers increases the effective contact area during impact compared with randomly oriented nanofiber mats, thereby enhancing triboelectric performance.[63] In addition, CNC incorporation further improved the electrical properties of PVDF-HFP-based TENGs. The output performance increased with CNC content, reaching maximum values at 1.0 wt % CNC: an open-circuit voltage of 281.3 V, a short-circuit current of 57.0 μA, and a transferred charge of 95 nC. Beyond this concentration, V_{OC}, I_{SC}, and transferred charge all decreased. Notably, although the β-phase content slightly decreased with CNC addition, the CNC/PVDF-HFP-based TENG still exhibited superior performance compared with the pristine PVDF-HFP-based device. For the CNC/PVDF-HFP-based TENGs, the differences in CPD and Φ between the TPU layer and the CNC/PVDF-HFP layer increased with increasing CNC content, facilitating enhanced charge generation during the contact−separation cycles. Consequently, the V_{OC}, I_{SC}, and transferred charge values of the CNC/PVDF-HFP-based TENGs were higher than those of the pristine PVDF-HFP-based TENG. However, excessive CNC loading reduces β-phase content and disrupts molecular chain alignment, ultimately lowering surface charge density and deteriorating output performance. In addition, the diameter of the PVDF-HFP fibers increased with increasing CNC content, resulting in a reduced contact area between the TPU and CNC/PVDF-HFP nanofibrous membranes. Moreover, the aggregation of CNCs results in a lower dielectric constant for the CNC/PVDF-HFP membranes with 1.5 and 2.0 wt % CNC. Consequently, the V_{OC}, I_{SC}, and transferred charge values of the APCNC-1.5- and APCNC-2.0-based TENGs were not higher than those of APCNC-1.0, even though the APCNC-1.5 and APCNC-2.0 films exhibited smaller CPD values and lower Φ compared to the APCNC-1.0 film.

The molecular interactions between CNCs and PVDF-HFP affect the triboelectric performance of the composite membranes. Hydrogen bonding, dipole−dipole interactions, and van der Waals forces facilitate strong interfacial adhesion and uniform CNC dispersion. The interactions between CNC and PVDF-HFP results were evidenced by X-ray photoelectron spectroscopy (Figure S18). Compared with the pristine PVDF-HFP membrane, the F 1s peak of PVDF-HFP was slightly

https://doi.org/10.1021/acsaem.5c03103
ACS Appl. Energy Mater. 2025, 8, 17530−17543

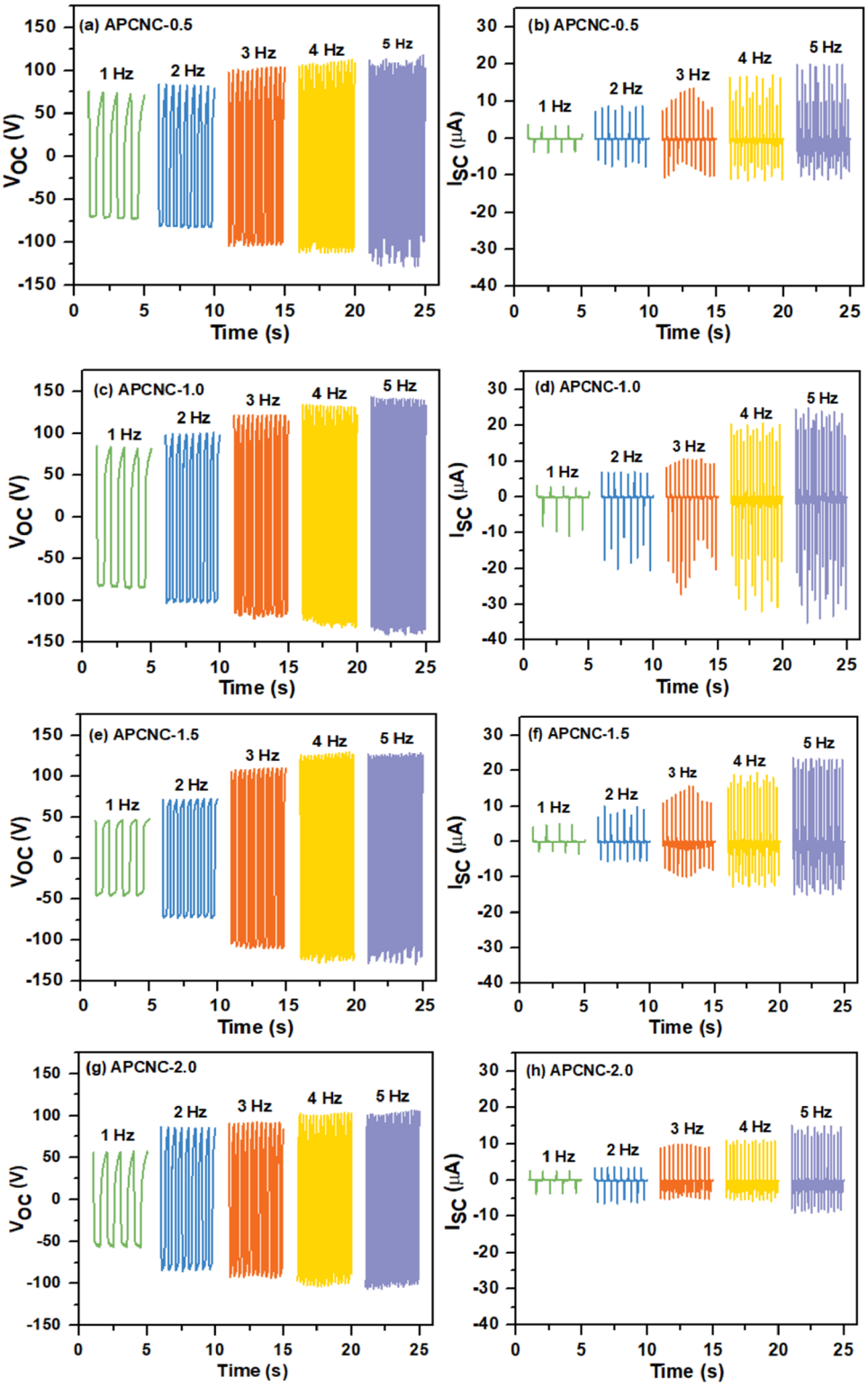

Figure 9. V_{OC} and I_{SC} of the TENGs measured at 50 N under various applied frequencies [(a), (b): APCNC-0.5 TENG; (c), (d): APCNC-1.0 TENG; (e), (f): APCNC-1.5 TENG; (g), (h): APCNC-2.0 TENG].

affected by the presence of CNCs in the APCNC-1.0 sample. Moreover, the intensity of the O 1s peak originating from CNCs decreased and shifted to a lower binding energy in the APCNC-1.0 sample.

Compared with the pristine PVDF-HFP-based TENG, the enhancement in the electrical properties of the CNC/PVDF-HFP-based TENGs arises from several synergistic effects. First, CNCs possess intrinsic piezoelectricity arising from their asymmetric crystalline structure. When incorporated into PVDF-HFP, CNCs can enhance dipole alignment and improve both dielectric and piezoelectric responses, thereby enabling the composite to store more charges during contact–separation cycles.[64,65] Second, the additional electron-trapping sites provided by CNC, which facilitate charge accumulation in

https://doi.org/10.1021/acsaem.5c03103
ACS Appl. Energy Mater. 2025, 8, 17530−17543

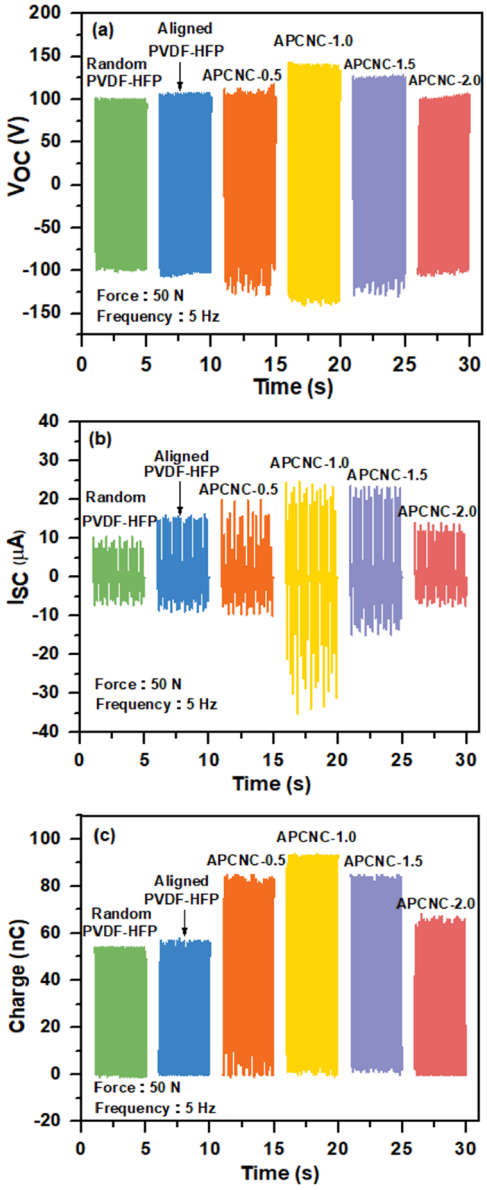

Figure 10. Electric properties of the random PVDF-HFP, aligned PVDF-HFP, and CNC/PVDF-HFP composite films based TENGs measured at 5 Hz under applied force of 50 N [(a) V_{OC}, (b) I_{SC}, and (c) transfer charge].

the electro-spun fibers. Moreover, under contact−separation operation, CNCs align along the electrode direction, generating a net electric field that increases the Fermi-level difference, thereby promoting electron transfer to the surface and enhancing surface charge density.[32,66] Third, CNCs can enhance the mechanical flexibility and stress distribution of the membranes, enabling more effective deformation under applied forces, which could greatly enhance the piezoelectric performance of CNC incorporated composite membranes.[67] Collectively, these effects explain the observed improvement in triboelectric output with optimal CNC loading.

To gain a deeper understanding of the potential distribution during TENG operation, the potential distribution between the positive and negative triboelectric layers at different separation distances was studied using COMSOL simulation, as shown in Figure 11. The simulation parameters are summarized in Table S6. In the initial state, the APCNC-1.0

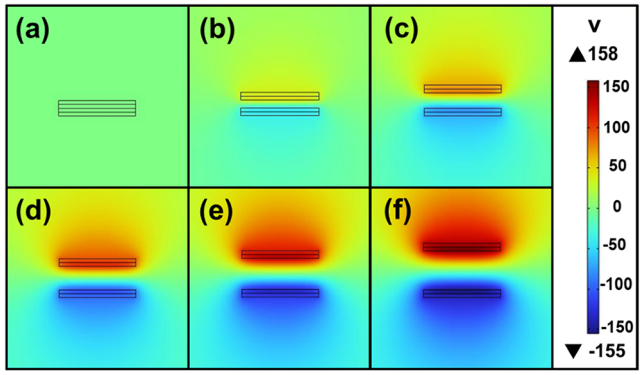

Figure 11. COMSOL simulation results of the potential distribution in the APCNC-1.0 TENG with various separation distances [(a) 0 mm, (b) 2 mm, (c) 4 mm, (d) 6 mm, (e) 8 mm, and (f) 10 mm].

TENG reached electrostatic equilibrium. As the separation distance between the two layers increased, the surface potential difference increased with distance. When the separation distance reached 10 mm, the voltage gradually increased from 0 to 313.0 V. The simulated V_{OC} closely matched the experimentally measured value, confirming that the mechanical energy generated during vertical contact−separation of the triboelectric layers can be effectively converted into electrical energy.

At an applied force of 50 N and applied frequency of 5 Hz and, the APCNC-1.0-based TENG was connected to various external load resistances, and its electrical output was measured over a resistance range from 1 Ω to 1 GΩ. As shown in Figure 12a,b, with increasing external load resistance, the V_{OC} of the TENG increased, while the I_{SC} showed a decreasing trend. The maximum output power density of 5.92 W/m^2 was achieved at a load resistance of 19.3 MΩ. As shown in Figure 12c, the output voltage of the APCNC-1.0-based TENG was monitored after 18,000 continuous contact−separation cycles. The results indicate that the V_{OC} remained at approximately 300 V even after repeated impacts, demonstrating the excellent cycling durability and stability of the APCNC-1.0-based TENG.

As summarized in Table S7, CNC and maleic anhydride−modified CNC (M-CNC) have been incorporated into gelatin, methylcellulose (MC) films, and epoxidized natural rubber (ENR) to form solid films serving as the positive friction layer in TENGs. The output electronic performance of APCNC-1.0 was superior to that of these CNC-based TENGs.[25,31,33] Furthermore, the performance of APCNC-1.0 also exceeded that of TENGs reported in the literature that were fabricated using CNC/PVDF nanofibrous membranes as the negative friction layer.[68] In addition, polymers (P3HT, PAN, and PMMA), nanocarbon materials (CNTs, rGO, graphene, and graphene quantum dots), MXene, metals, transition metal oxides, metal sulfides, metal nitrides, and metal hydroxides have been incorporated into PVDF, PVDF-HFP, and PVDF-TrFE nanofibrous membranes to enhance the output electronic performance of TENGs (Table S8). Nevertheless, the output performance of the APCNC-1.0−based TENG was found to be comparable to, or even superior to, that of these reported TENGs.[22,69−87]

3.9. Application of the APCNC-1.0-Based TENG. To enable the TENG to drive wearable devices and operate continuously, a bridge rectifier was used as an AC-to-DC converter and connected to a capacitor as an energy storage

https://doi.org/10.1021/acsaem.5c03103
ACS Appl. Energy Mater. 2025, 8, 17530−17543

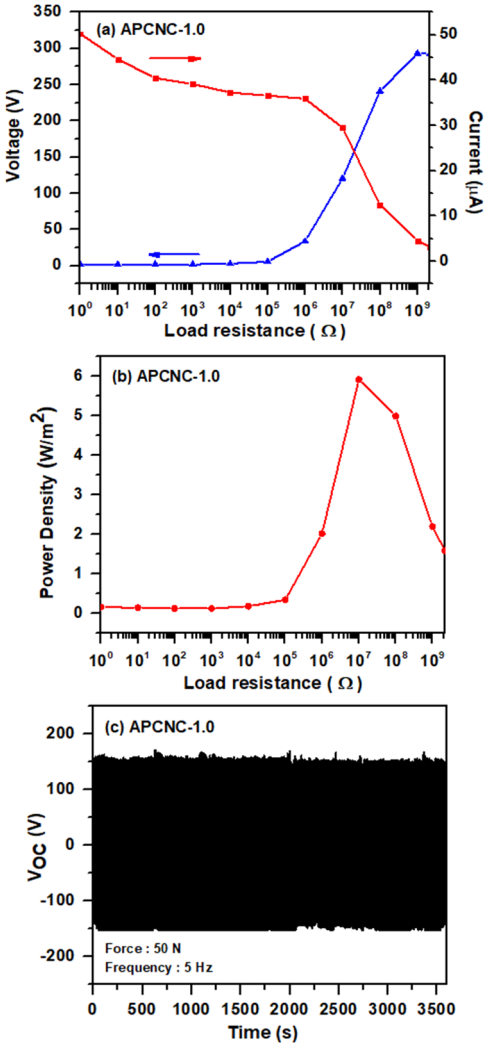

Figure 12. (a) Output and voltage current of TENG with various external load resistances, (b) dependence of output power on load resistances, and (c) durability test of the APCNC-1.0 based TENG under 50 N pressure and 5 Hz for 18,000 cycles.

device, thereby forming a self-powered system. As shown in Figure S19, the APCNC-1.0-based TENG was used to charge commercial electrolytic capacitors with capacitances of 1, 10, and 100 μF. Under an applied force of 50 N and a contact frequency of 5 Hz, the 1 μF capacitor was charged to 35 V within approximately 70 s. As the capacitance increased, the charging rate gradually decreased.

To demonstrate the practical applicability of the high electrical output from the TENG in powering small electronic devices, the TENG was connected to a bridge rectifier and then linked in series with 100 commercial LEDs and LEDs arranged in the shape of "NCHU", as shown in Figure 13a,b. Under an applied force of 50 N and a contact frequency of 5 Hz, both the 100 commercial LEDs and the "NCHU"-pattern LEDs were simultaneously illuminated, confirming that the TENG effectively converts mechanical energy into electrical energy for driving electronic components. As shown in Figure 13c,d, the AC output from the TENG was rectified to DC power via a bridge rectifier to operate wearable devices. For continuous operation, a 100 μF commercial electrolytic capacitor was connected to store the TENG output. After approximately 3 min of charging, the capacitor voltage reached

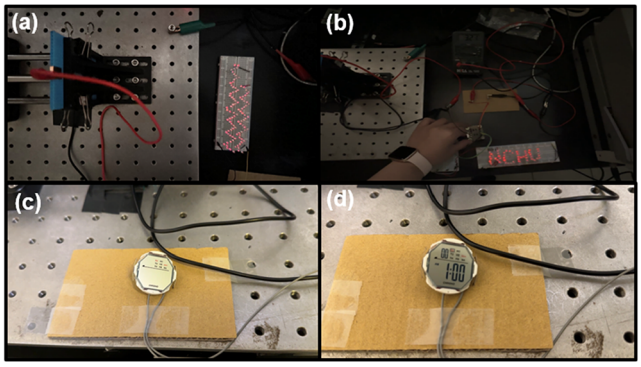

Figure 13. APCNC-1.0-based TENG powering (a) 100 commercial LEDs, (b) series-connected LEDs arranged in the shape of "NCHU", and (c, d) an electronic watch.

1.6 V, at which point the stored energy was used to power an electronic watch. The watch operated stably for about 1.5 min, demonstrating the TENG's capability to supply portable electronics.

4. CONCLUSION

Cellulose nanocrystal/poly(vinylidene fluoride)-*co*-hexafluoropropylene (CNC/PVDF-HFP) composite electrospun nanofibrous membranes were developed as the negative friction layer of the TENG. SEM images revealed that the aligned CNC/PVDF-HFP nanofibers exhibited well-defined unidirectional alignment, with fiber diameters progressively increasing from 300 to 1650 nm as the CNC content increased. EDX analyses further confirmed the uniform distribution of CNC particles throughout the PVDF-HFP nanofibrous matrix. The contact angle measurements showed a decrease with increasing CNC content, indicating enhanced hydrophilicity. X-ray diffraction results indicated that the β-phase content slightly decreased upon CNC incorporation. Nevertheless, the CNC/PVDF-HFP-based TENG exhibited markedly improved electrical performance compared with the pristine PVDF-HFP-based device. The introduction of dipolar CNC nanoparticles enhanced the dielectric constant of the CNC/PVDF-HFP membrane. Moreover, the work function differences between the TPU-based positive triboelectric layer and the CNC/PVDF-HFP-based negative triboelectric layer increased with higher CNC content, which facilitated enhanced charge generation during the contact−separation cycles. The output voltage of the APCNC-1.0-based TENG was monitored over 18,000 continuous contact−separation cycles, maintaining a stable V_{OC} of ∼300 V, which demonstrates its excellent cycling durability and stability. A maximum output power density of 5.92 W m^{-2} was achieved at an external load resistance of 19.3 MΩ. Furthermore, the CNC/PVDF-HFP-based TENG successfully powered small electronic devices, including LEDs and electronic watches.

■ ASSOCIATED CONTENT

Supporting Information

The Supporting Information is available free of charge at https://pubs.acs.org/doi/10.1021/acsaem.5c03103.

TGA and DSC thermograms; SEM and TEM images; diameter distributions of CNC/PVDF-HFP fibers; contact angle of CNC/PVDF-HFP nanofibrous membranes; FTIR spectrum and XRD images of TPU and

https://doi.org/10.1021/acsaem.5c03103
ACS Appl. Energy Mater. 2025, 8, 17530−17543

CNC/PVDF-HFP nanofibrous membranes; V_{OC} and I_{SC} of the CNC/PVDF-HFP based TENGs; charging of commercial capacitors by the APCNC-1.0-based TENG (PDF)

AUTHOR INFORMATION

Corresponding Author

Rong-Ho Lee − *Department of Chemical Engineering, National Chung Hsing University, Taichung 402, Taiwan; Graduate Institute of Precision Engineering, National Chung Hsing University, Taichung 40227, Taiwan;* orcid.org/0000-0002-1373-9360; Phone: +886-4-22854308; Email: rhl@dragon.nchu.edu.tw; Fax: +886-4-22854734

Authors

Hsin-Jung Kan − *Department of Chemical Engineering, National Chung Hsing University, Taichung 402, Taiwan*

Cheng-Hung Chi − *Department of Chemical Engineering, National Chung Hsing University, Taichung 402, Taiwan*

Ji-Wu Han − *Department of Chemical Engineering, National Chung Hsing University, Taichung 402, Taiwan*

Hongta Yang − *Department of Chemical Engineering, National Chung Hsing University, Taichung 402, Taiwan*

Shin-Chi Lai − *Department of Automation Engineering, National Formosa University, Yunlin 632301, Taiwan*

Po-Hsun Chen − *Department of Applied Materials and Optoelectronic Engineering, National Chi Nan University, Nantou 54561, Taiwan*

Po-Liang Liu − *Department of Applied Materials and Optoelectronic Engineering, National Chi Nan University, Nantou 54561, Taiwan; Department of Chemical Engineering and Materials Science, Yuan Ze University, Taoyuan City 320, Taiwan*

Complete contact information is available at: https://pubs.acs.org/10.1021/acsaem.5c03103

Author Contributions

Conceptualization: R.H.L.; Data curation: H.J.K, C.H.C., and J.W.H.; Writing—original draft preparation: R.H.L.; Writing—review and editing: R.H.L.; Visualization: R.H.L.; Supervision: H.Y., S.C.L., and R.H.L.; Project administration and funding acquisition: R.H.L. All authors have read and agreed to the published version of the manuscript.

Notes

The authors declare no competing financial interest.

ACKNOWLEDGMENTS

The authors thank the National Science and Technology Council (NSTC) of Taiwan (grant no. NSTC 113-2221-E-005-006) for financial support.

REFERENCES

(1) Wang, Z. L. Triboelectric nanogenerators as new energy technology for self-powered systems and as active mechanical and chemical sensors. *ACS Nano* **2013**, *7*, 9533−9557.

(2) Kınas, Z.; Karabiber, A.; Yar, A.; Ozen, A.; Ozel, F.; Ersoz, M.; Okbaz, A. High-performance triboelectric nanogenerator based on carbon nanomaterials functionalized polyacrylonitrile nanofibers. *Energy* **2022**, *239*, No. 122369.

(3) Kim, W. G.; Kim, D. W.; Tcho, I. W.; Kim, J. K.; Kim, M. S.; Choi, Y. K. Triboelectric Nanogenerator: Structure, mechanism, and applications. *ACS Nano* **2021**, *15*, 258−287.

(4) Sun, F.; Zhu, Y.; Jia, C.; Ouyang, B.; Zhao, T.; Li, C.; Ba, N.; Li, X.; Chen, S.; Che, T.; Mao, Y. A flexible lightweight triboelectric nanogenerator for protector and scoring system in taekwondo competition monitoring. *Electronics* **2022**, *11*, No. 1306.

(5) Zhang, W.; Liu, Q.; Chao, S.; Liu, R.; Cui, X.; Sun, Y.; Ouyang, H.; Li, Z. Ultrathin stretchable triboelectric nanogenerators improved by postcharging electrode material. *ACS Appl. Mater. Interfaces* **2021**, *13*, 42966−42976.

(6) Jiang, Y.; Dong, K.; Li, X.; An, J.; Wu, D.; Peng, X.; Yi, J.; Ning, C.; Cheng, R.; Yu, P.; Wang, Z. L. Stretchable, washable, and ultrathin triboelectric nanogenerators as skin-like highly sensitive self-powered haptic sensors. *Adv. Funct. Mater.* **2021**, *31*, No. 2005584.

(7) Doganay, D.; Cicek, M. O.; Durukan, M. B.; Altuntasf, B.; Agbahca, E.; Coskun, S.; Unalan, H. E. Fabric based wearable triboelectric nanogenerators for human machine interface. *Nano Energy* **2021**, *89*, No. 106142.

(8) Sun, W.; Luo, N.; Liu, Y.; Li, H.; Wang, D. A new self-healing triboelectric nanogenerator based on polyurethane coating and its application for self-powered cathodic protection. *ACS Appl. Mater. Interfaces* **2022**, *14*, 10498−10507.

(9) Cheng, K.; Huang, Z.; Wang, P.; Sun, L.; Ghasemi, H.; Ardebili, H.; Karim, A. Antibacterial flexible triboelectric nanogenerator via capillary force lithography. *J. Colloid Interface Sci.* **2023**, *630*, 611−622.

(10) Abir, S. S. H.; Sadaf, M. U.; Saha, S. K.; Touhami, A.; Lozano, K.; Uddin, M. J. Nanofiber-based substrate for a triboelectric nanogenerator: high-performance flexible energy fiber mats. *ACS Appl. Mater. Interfaces* **2021**, *13*, 60401−60412.

(11) Joo, H.; Gwak, S.; Lee, M. H.; Park, H.; Lee, C.; Lee, J. H.; Han, S. A.; Lee, J. H. Functionalized thermoplastic polyurethane with tunable tribopolarity and biodegradability for high performance and biodegradable triboelectric nanogenerator. *Sustainale Mater. Technol.* **2023**, *36*, No. e00638.

(12) Doganay, D.; Cicek, M. O.; Durukan, M. B.; Altuntasf, B.; Agbahca, E.; Coskun, S.; Unalan, H. E. Fabric based wearable triboelectric nanogenerators for human machine interface. *Nano Energy* **2021**, *89*, No. 106412.

(13) Chinya, I.; Pal, A.; Sen, S. Flexible, hybrid nanogenerator based on zinc ferrite nanorods incorporated poly(vinylidene fluoride-co-hexafluoropropylene) nanocomposite for versatile mechanical energy harvesting. *Mater. Res. Bull.* **2019**, *118*, No. 110515.

(14) He, Y. L.; Wang, H. Y.; Sha, Z.; Boyer, C.; Wang, H.; Zhang, J. Enhancing output performance of PVDF-HEP fiber-based nanogenerator by hybridizing silver nanowires and perovskite oxide nanocrystals. *Nano Energy* **2022**, *98*, No. 107343.

(15) Lee, J. E.; Shin, Y. E.; Lee, G. H.; Kim, J.; Ko, H.; Chae, H. G. Polyvinylidene fluoride (PVDF)/cellulose nanocrystal (CNC) nanocomposite fiber and triboelectric textile sensors. *Composites, Part B* **2021**, *223*, No. 109098.

(16) Li, Y.; Xiong, J.; Lv, J.; Chen, J.; Gao, D.; Zhang, X.; Lee, P. S. Mechanically interlocked stretchable nanofibers for multifunctional wearable triboelectric nanogenerator. *Nano Energy* **2020**, *78*, No. 105358.

(17) Yu, Y.; Wu, H.; Yu, Y. L.; Yan, J.; Shi, J.; Morikawa, H.; Lyu, W.; Zhu, C. Acid- and alkali-resistant, UV-shielding, and photocatalytic self-cleaning nanofiber membrane-based wearable triboelectric nanogenerator for ultra-low-frequency energy-harvesting and self-powered sensors. *Chem. Eng. J.* **2024**, *490*, No. 151546.

(18) Ngadong, S.; Chekke, T.; Narzary, R.; Bayan, S.; Das, U. Metal oxide nanocomposite based flexible nanogenerator: synergic effect of light and pressure. *Nanotechnology* **2023**, *34*, No. 045403.

(19) Zhi, C.; Zhang, S.; Wu, H.; Ming, Y.; Shi, S.; Io, W. F.; Meng, S.; Si, Y. F.; Fei, B.; Hao, J.; Hu, J. Perovskite nanocrystals induced core−shell inorganic−organic nanofibers for efficient energy harvesting and self-powered monitoring. *ACS Nano* **2024**, *18*, 9365−9377.

(20) Saikh, M. M.; Hoque, N. A.; Biswas, P.; Rahman, W.; Das, N.; Das, S.; Thakur, P. ZrO_2/poly(vinylidene fluoride-co-hexafluoropropylene) nanocomposite-based piezoelectric nanogenerator and single-

electrode triboelectric nanogenerator for sustainable energy harvesting from human movements. *Phys. Status Solidi A* **2021**, *218*, No. 200695.
(21) Manchi, P.; Graham, S. A.; Patnam, H.; Paranjape, M. V.; Yu, J. S. High-efficiency poly(vinylidene fluoride-co-hexafluoropropylene) loaded 3D marigold flower-like bismuth tungstate triboelectric films for mechanical energy harvesting and sensing applications. *Small* **2022**, *18*, No. 2200822.
(22) Im, J. S.; Park, I. K. Mechanically robust magnetic Fe_3O_4 nanoparticle/polyvinylidene fluoride composite nanofiber and its application in a triboelectric nanogenerator. *ACS Appl. Mater. Interfaces* **2018**, *10*, 25660−25665.
(23) Shao, Y.; Luo, B.; Liu, T.; Cai, C.; Meng, X.; Wang, S.; Nie, S. Harvesting energy from extreme environmental conditions with cellulosic triboelectric materials. *Mater. Today* **2023**, *66*, 348−370.
(24) Song, Y. H.; Shi, Z. Q.; Hu, G. H.; Xiong, C. X.; Isogai, A.; Yang, Q. L. Recent advances in cellulose-based piezoelectric and triboelectric nanogenerators for energy harvesting: a review. *J. Mater. Chem. A* **2021**, *9*, 1910−1937.
(25) Somseemee, O.; Siriwong, K.; Sae-Oui, P.; Harnchana, V.; Appamato, I.; Prada, T.; Siriwong, C. Preparation of UV-cured cellulose nanocrystal-filled epoxidized natural rubber and its application in a triboelectric nanogenerator. *Int. J. Biol. Macromol.* **2024**, *262*, No. 130109.
(26) Sonker, A. K.; Kumar, C.; Tideland, H.; Bairagi, S.; Katiyar, N. K.; Mulvihill, D. M.; Westman, G. Bendable substrates of cellulose nanocrystals for triboelectric nanogenerators. *ACS Appl. Nano Mater.* **2025**, *8*, 9868−9877.
(27) Zhou, J.; Wang, H.; Du, C.; Zhang, D.; Lin, H.; Chen, Y.; Xiong, J. Cellulose for sustainable triboelectric nanogenerators. *Adv. Energy Sustainability Res.* **2022**, *3*, No. 2100161.
(28) Teng, C. P.; Tan, M. Y.; Toh, J. P.; Lim, Q. F.; Wang, X.; Ponsford, D.; Lin, E. M. J. R.; Thitsartarn, W.; Tee, S. Y. Advances in cellulose-based composites for energy applications. *Materials* **2023**, *16*, No. 3856.
(29) Wei, Z.; Wang, J.; Liu, Y.; Yuan, J.; Liu, T.; Du, G.; Zhu, S.; Nie, S. Sustainable triboelectric materials for smart active sensing systems. *Adv. Funct. Mater.* **2022**, *32*, No. 2208277.
(30) Nie, S.; Cai, C.; Lin, X.; Zhang, C. Y.; Lu, Y.; Mo, J.; Wang, S. F. Chemically functionalized cellulose nanofibrils for improving triboelectric charge density of a triboelectric nanogenerator. *ACS Sustainable Chem. Eng.* **2020**, *8*, 18678−18685.
(31) Wang, T.; Li, S.; Tao, X.; Yan, Q.; Wang, X. L.; Chen, Y.; Huang, F.; Li, H.; Chen, X. Y.; Bian, Z. F. Fully biodegradable water-soluble triboelectric nanogenerator for human physiological monitoring. *Nano Energy* **2022**, *93*, No. 106787.
(32) Peng, J.; Zhang, H. L.; Zheng, O. F.; Clemons, C. M.; Sabo, R. C.; Gong, S.; Mac, Z. Q.; Turng, L. S. A composite generator film impregnated with cellulose nanocrystals for enhanced triboelectric performance. *Nanoscale* **2017**, *9*, 1428−1433.
(33) Su, Z.; Ma, X. A triboelectric nanogenerator based on CNC/gelatin for running and jumping training monitoring. *AIP Adv.* **2024**, *14*, No. 015348.
(34) Alghamdi, M. S.; Morgan, J. J.; Walsh, K.; Shin, D. W.; Nigmatullin, R.; Saadi, Z.; Routledge, J.; Neves, A. I. S.; Russo, S.; Eichhorn, S. J.; Craciun, M. F. Triboelectric nanogenerator based on cellulose nanocrystals and graphene for energy harvesting from piano playing motion. *Nano Energy* **2025**, *138*, No. 110816.
(35) Huang, J.; Zhang, Y.; Yu, H.; Han, G.; Cheng, W. Cellulose-based triboelectric nanogenerator prepared by multi-fluid electrospinning for respiratory protection and self-powered sensing. *Actuators* **2024**, *13*, No. 178.
(36) Sha, Z.; Boyer, C.; Li, G.; Yu, Y.; Allioux, F. M.; Zadeh, K. K.; Wang, C. H.; Zha, J. Electrospun liquid metal/PVDF-HFP nanofiber membranes with exceptional triboelectric performance. *Nano Energy* **2022**, *92*, No. 106713.
(37) Persano, L.; Dagdeviren, C.; Su, Y. W.; Zhang, Y.; Girardo1, S.; Pisignano, D.; Huang, Y. G.; Rogers, J. A. High performance piezoelectric devices based on aligned arrays of nanofibers of poly(vinylidenefluoride-co-trifluoroethylene). *Nat. Commun.* **2013**, *4*, No. 1633.
(38) Khandelwal, G.; Min, G.; Karagiorgis, X.; Dahiya, R. Aligned PLLA electrospun fibres based biodegradable triboelectric nanogenerator. *Nano Energy* **2023**, *110*, No. 108325.
(39) Kresse, G.; Furthmu¨ller, J. Efficient iterative schemes for ab initio total-energy calculations using a plane-wave basis set. *Phys. Rev. B* **1996**, *54*, 11169−11186.
(40) Kresse, G.; Furthmu¨ller, J. Efficiency of ab-initio total energy calculations for metals and semiconductors using a plane-wave basis set. *Comput. Mater. Sci.* **1996**, *6*, 15−50.
(41) Kresse, G.; Furthmu¨ller, J. Norm-conserving and ultrasoft pseudopotentials for first-row and transition elements. *J. Phys.:-Condens. Matter* **1994**, *6*, 45−8257.
(42) Kresse, G.; Joubert, D. From ultrasoft pseudopotentials to the projector augmented-wave method. *Phys. Rev. B* **1999**, *59*, 1758−1775.
(43) Perdew, J. P.; Chevary, J. A.; Vosko, S. H.; Jackson, K. A.; Pederson, M. R.; Singh, D. J.; Fiolhais, C. Atoms, molecules, solids, and surfaces: Applications of the generalized gradient approximation for exchange and correlation. *Phys. Rev. B* **1992**, *46*, 6671−6687.
(44) Gong, J.; Li, J.; Xu, J.; Xiang, Z.; Mo, L. Research on cellulose nanocrystals produced from cellulose sources with various polymorphs. *RSC Adv.* **2017**, *7*, 33486−33493.
(45) Feng, Y. C.; Cai, C. E.; Liu, B. T.; Yang, H.; Lee, R. H. Cellulose nanocrystal-incorporated $MAPbI_3$ for inverted perovskite solar cells with enhanced efficiency and stability. *ACS Appl. Energy Mater.* **2024**, *7*, 12092−12102.
(46) Mbakop, S.; Nthunya, L. N.; Onyango, M. S. Recent advances in the synthesis of nanocellulose functionalized−hybrid membranes and application in water quality improvement. *Processes* **2021**, *9*, No. 611.
(47) Arik, N.; Horzum, N.; Truong, Y. B. Development and characterizations of engineered electrospun bio-based polyurethane containing essential oils. *Membranes* **2022**, *12*, No. 209.
(48) PBoruah, P.; Gupta, R.; Katiyar, V. Fabrication of cellulose nanocrystal (CNC) from waste paper for developing antifouling and high-performance polyvinylidene fluoride (PVDF) membrane for water purification. *Carbohydr. Polym. Technol. Appl.* **2023**, *5*, No. 100309.
(49) Chieng, B. W.; Lee, S. H.; Ibrahim, N. A.; Then, Y. Y.; Loo, Y. Y. Isolation and characterization of cellulose nanocrystals from oil palm mesocarp fiber. *Polymers* **2017**, *9*, No. 355.
(50) Khalili, H.; Salim, M. H.; Tlemcani, S. E. J.; Makhlouf, R.; Hassani, F. Z. S. A.; Ablouh, H.; Kassab, Z.; Achaby, M. E. Bio-nanocomposite films based on cellulose nanocrystals filled polyvinyl alcohol/alginate polymer blend. *J. Fibers Polym. Compos.* **2022**, *1*, 77−96.
(51) Hemmati, F.; Jafari, S. M.; Taheri, R. A. Optimization of homogenization-sonication technique for the production of cellulose nanocrystals from cotton linter. *Int. J. Biol. Macromol.* **2019**, *137*, 374−381.
(52) Shekh, M. I.; Wang, M.; Zhu, G.; Stadler, F. J.; Ma, J.; Du, B. Mechanically robust and conductive zwitter ionic polymer coated electrospun nanofibrous electrolyte membranes for wireless human motion detection and capacitor applications. *Compos. Struct.* **2024**, *329*, No. 117797.
(53) Yang, J.; Wang, M.; Meng, Y.; Niu, Z.; Hao, Y.; Liu, H.; Su, W.; Zhang, H.; Qin, Y.; Zhang, C.; Li, X. High-Performance flexible wearable triboelectric nanogenerator sensor by β-phase polyvinylidene fluoride polarization. *ACS Appl. Electron. Mater.* **2024**, *6*, 1385−1395.
(54) Gao, M.; Wang, C.; Zhu, L.; Cheng, Q.; Xu, X.; Xu, G.; Huang, Y.; Bao, J. Composite polymer electrolytes based on electrospun thermoplastic polyurethane membrane and polyethylene oxide for all-solid-state lithium batteries. *Polym. Int.* **2019**, *68*, 1538−1539.
(55) Beniwal, A.; Sunny. Novel TPU/Fe_2O_3 and TPU/Fe_2O_3/PPy nanocomposites synthesized using electrospun nanofibers investigated for analyte sensing applications at room temperature. *Sens. Actuators, B* **2020**, *304*, No. 127384.

https://doi.org/10.1021/acsaem.5c03103
ACS Appl. Energy Mater. 2025, 8, 17530−17543

(56) Tomer, V.; Manias, E.; Randall, C. A. High field properties and energy storage in nanocomposite dielectrics of poly(vinylidene fluoride-hexafluoropropylene). *J. Appl. Phys.* **2011**, *110*, No. 044107.
(57) Parangusan, H.; Deepalekshmi, P.; Mariam, M. A. A. A. Stretchable electrospun PVDF-HFP/Co-ZnO nanofibers as piezoelectric nanogenerators. *Sci. Rep.* **2018**, *8*, No. 754.
(58) Tohluebaji, N.; Thainiramit, P.; Putson, C.; Muensit, N. Phase and structure behavior vs electromechanical performance of electrostrictive P(VDF-HFP)/ZnO composite nanofibers. *Polymers* **2021**, *13*, No. 2565.
(59) Kim, M. P.; Um, D. S.; Shin, Y. E.; Ko, H. High-performance triboelectric devices via dielectric polarization: A review. *Nanoscale Res. Lett.* **2021**, *16*, No. 35.
(60) Wang, D. C.; Guo, H.; Wang, P.; Li, J.; Sun, Y.; Zhang, D. An advanced strategy to enhance TENG output: Reducing triboelectric charge. *Adv. Mater.* **2023**, *35*, No. 2209895.
(61) Rana, S. M. S.; Rahman, M. T.; Salauddin, M.; Sharma, S.; Maharjan, P.; Bhatta, T.; Cho, H.; Park, C.; Park, J. Y. Electrospun PVDF-TrFE/MXene nanofiber mat-based triboelectric nanogenerator for smart home appliances. *ACS Appl. Mater. Interfaces* **2021**, *13*, 4955−4967.
(62) Hao, Y.; Wen, J.; Gao, X.; Nan, D.; Pan, J.; Yang, Y.; Chen, B.; Wang, Z. L. Self-rebound cambered triboelectric nanogenerator array for self-powered sensing in kinematic analytics. *ACS Nano* **2022**, *16*, 1271−1279.
(63) Rastegardoost, M. M.; Tafreshi, O. A.; Saadatnia, Z.; Ghaffari-Mosanenzadeh, S.; Park, C. B.; Naguib, H. E. Porous PVDF mats with significantly enhanced dielectric properties and novel dipole arrangement for high-performance triboelectric nanogenerators. *Appl. Mater. Today* **2023**, *30*, No. 101732.
(64) Csoka, L.; Hoeger, I. C.; Rojas, O. J.; Peszlen, I.; Pawlak, J. J.; Peralta, P. Piezoelectric effect of cellulose nanocrystals thin films. *ACS Macro Lett.* **2012**, *1*, 318−323.
(65) Wang, J.; Carlos, C.; Zhang, Z.; Li, J.; Long, Y.; Yang, F.; Dong, Y.; Qiu, X.; Qian, Y.; Wang, X. Piezoelectric nanocellulose thin film with large-scale vertical crystal alignment. *ACS Appl. Mater. Interfaces* **2020**, *12*, 26399−26404.
(66) Wang, N.; Yang, D.; Zhang, W.; Feng, M.; Li, Z.; Ye, F.; Loh, X. J.; Wang, D. Deep trap boosted ultrahigh triboelectric charge density in nanofibrous cellulose-based triboelectric nanogenerators. *ACS Appl. Mater. Interfaces* **2023**, *15*, 997−1009.
(67) Sun, B.; Chao, D.; Wang, C. Pizoelectric nanogenerator based on electrospun cellulose acetate/nanocellulose crystal composite membranes for energy harvesting application. *Chem. Res. Chin.Univ.* **2002**, *38*, 1005−1011.
(68) Fashandi, H.; Abolhasani, M. M.; Sandoghdar, P.; Zohdi, N.; Li, Q.; Naebe, M. Morphological changes towards enhancing piezoelectric properties of PVDF electrical generators using cellulose nanocrystals. *Cellulose* **2016**, *23*, 3625−3637.
(69) Lin, M. F.; Chang, K. W.; Lee, C. H.; Wu, X. X.; Huang, Y. C. Electrospun P3HT/PVDF-HFP semiconductive nanofibers for triboelectric nanogenerators. *Sci. Rep.* **2022**, *12*, No. 14842.
(70) Shao, H.; Wang, H.; Cao, Y.; Ding, X.; Bai, R.; Chang, H.; Fang, J.; Jin, X.; Wang, W.; Lin, T. Single-layer piezoelectric nanofiber membrane with substantially enhanced noise-to-electricity conversion from endogenous triboelectricity. *Nano Energy* **2021**, *89*, No. 106427.
(71) Deng, X.; Wu, Z.; Yu, X.; Wang, M.; Zang, D.; Long, Y.; Guo, N.; Weng, L.; Liu, Y.; Gao, J. Preparation and properties of triboelectric nanogenerator based on PVDF-TrFE/PMMA electrospun film. *Adv. Compos. Hybrid Mater.* **2025**, *8*, No. 19.
(72) Lan, L.; Xiong, J.; Gao, D.; Li, Y.; Chen, J.; Lv, J.; Ping, J.; Ying, Y.; Lee, P. S. Breathable nanogenerators for an on-plant self-powered sustainable agriculture system. *ACS Nano* **2021**, *15*, 5307−5315.
(73) Huang, T.; Yu, H.; Wang, H.; Zhang, Q.; Zhu, M. Hydrophobic SiO_2 electret enhances the performance of poly(vinylidene fluoride) nanofiber-based triboelectric nanogenerator. *J. Phys. Chem. C* **2016**, *120*, 26600−26608.
(74) Choi, G. J.; Baek, S. H.; Lee, S. S.; Khan, F.; Kim, J. H.; Park, I. K. Performance enhancement of triboelectric nanogenerators based on polyvinylidene fluoride/graphene quantum dot composite nanofibers. *J. Alloys Compd.* **2019**, *797*, 945−951.
(75) Huang, J.; Hao, Y.; Zhao, M.; Li, W.; Huang, F.; Wei, Q. All-fiber-structured triboelectric nanogenerator via one-pot electrospinning for self-powered wearable sensors. *ACS Appl. Mater. Interfaces* **2021**, *13*, 24774−24784.
(76) Cheon, S.; Kang, H.; Kim, H.; Son, Y.; Lee, J. Y.; Shin, H. J.; Kim, S. W.; Cho, J. H. High-performance triboelectric nanogenerators based on electrospun polyvinylidene fluoride−silver nanowire composite nanofibers. *Adv. Funct. Mater.* **2018**, *28*, No. 1703778.
(77) Liu, Q.; Wang, X. X.; Song, W. Z.; Qiu, H. J.; Zhang, J.; Fan, Z.; Yu, M.; Long, Y. Z. Wireless single-electrode self-powered piezoelectric sensor for monitoring. *ACS Appl. Mater. Interfaces* **2020**, *12*, 8288−8295.
(78) Kim, H. S.; Park, I. K. Enhanced output power from triboelectric nanogenerators based on electrospun Eu-doped polyvinylidene fluoride nanofibers. *J. Phys. Chem. Solids* **2018**, *117*, 188−193.
(79) Li, X.; Ji, D.; Yu, B.; Ghosh, R.; He, J.; Qin, X.; Ramakrishna, S. Boosting piezoelectric and triboelectric effects of PVDF nanofiber through carbon-coated piezoelectric nanoparticles for highly sensitive wearable sensors. *Chem. Eng. J.* **2021**, *426*, No. 130345.
(80) Venkatesan, H. M.; Arun, A. P. High-performance triboelectric nanogenerators based on Ag doped ZnO loaded electrospun PVDF nanofiber mats for energy harvesting and healthcare monitoring. *Sci. Rep.* **2025**, *15*, No. 3347.
(81) Motora, K. G.; Wu, C. M.; Rani, G. M.; Yen, W. T. Effect of ZnO particle size on piezoelectric nanogenerators and mechanical energy harvesting. *Express Polym. Lett.* **2022**, *16*, 1208−1227.
(82) He, S.; Gui, Y.; Wang, Y.; Yang, J. A self-powered β-$Ni(OH)_2$/MXene based ethanol sensor driven by an enhanced triboelectric nanogenerator based on β-$Ni(OH)_2$@PVDF at room temperature. *Nano Energy* **2023**, *107*, No. 108132.
(83) Venkatesan, H. M.; Arun, A. P. Nickel-oxide-doped polyvinylidene fluoride nanofiber-based flexible triboelectric nanogenerator for energy harvesting and healthcare monitoring applications. *ACS Appl. Electron. Mater.* **2024**, *6*, 1161−1173.
(84) Amrutha, B.; Yoon, J. U.; Woo, I.; Gajula, P.; Prabu, A. A.; Bae, J. W. Performance optimization of MoS_2-doped PVDF-HFP nanofiber triboelectric nanogenerator as sensing technology for smart cities. *Appl. Mater. Today* **2024**, *41*, No. 102503.
(85) Sun, C.; Zu, G.; Wei, Y.; Song, X.; Yang, X. Flexible triboelectric nanogenerators based on electrospun poly(vinylidene fluoride) with MoS_2/carbon nanotube composite nanofibers. *Langmuir* **2022**, *38*, 1479−1487.
(86) Zhou, y.; Tao, X.; Wang, Z.; An, M.; Qi, K.; Ou, K.; He, J.; Wang, R.; Chen, X.; Dai, Z. Electret-doped polarized nanofiber triboelectric nanogenerator with enhanced electrical output performance based on a micro-waveform structure. *ACS Appl. Electron. Mater.* **2022**, *4*, 2473−2480.
(87) Venkatesan, H. M.; Woo, I.; Yoon, J. U.; Gajula, P.; Arun, A. P.; Bae, J. W. Unveiling the latent potential: Ni/$CoFe_2O_4$-loaded electrospun PVDF hybrid composite-based triboelectric nanogenerator for mechanical energy harvesting applications. *Adv. Compos. Hybrid Mater.* **2025**, *8*, No. 221.

https://doi.org/10.1021/acsaem.5c03103
ACS Appl. Energy Mater. 2025, 8, 17530−17543